Detector performance of the space-borne Doppler wind LiDAR aboard the Aeolus satellite

Oliver Lux*[a], Robert Reichert[b], Christian Lemmerz[a], Nafiseh Masoumzadeh**[a], Denny Wernham[b], Trismono Candra Krisna[b], Denis Marchais[c], Ray Bell[d], Tommaso Parrinello[e], Oliver Reitebuch[a]
[a]Deutsches Zentrum für Luft- und Raumfahrt, Institut für Physik der Atmosphäre, Oberpfaffenhofen, Germany; [b]European Space Agency-ESTEC, Keplerlaan 1, Noordwijk, NL-2201AZ, The Netherlands; [c]Airbus Defence and Space, Toulouse, France; [d]Teledyne e2v, Chelmsford, United Kingdom; [e]European Space Research Institute, European Space Agency, Frascati, Italy

ABSTRACT

The European Space Agency's Aeolus mission (2018–2023) was the first to provide global wind measurements in near-real time using spaceborne Doppler wind lidar. Its instrument, the Atmospheric Laser Doppler Instrument (ALADIN), significantly advanced weather forecasting and atmospheric research. A persistent challenge during the mission was the presence of hot pixels on ALADIN's CCD detectors, which caused dark current anomalies and compromised wind data quality. These effects, often observed as random telegraph signals (RTS) and abrupt shifts in median dark current levels, required rigorous correction strategies. To address these issues, up to eight dark current calibrations were performed daily, resulting in an extensive dataset used to identify, monitor, and statistically characterize hot pixel behavior throughout the mission. This study presents a comprehensive analysis of hot pixels, including new insights into the correlation between RTS transition rates and amplitudes, and between activation energies and dark current rates. These analyses not only improved the accuracy of Aeolus wind products during reprocessing but also deepened understanding of CCD detector behavior in space environments. Dedicated end-of-life tests in 2023 further clarified the temperature dependence of dark currents and the origins of hot pixels. The results have direct implications for future Doppler lidar missions such as EarthCARE and Aeolus-2, as well as for other satellite systems employing CCD-based sensors.

Keywords: Doppler wind lidar, satellite, detectors, charge-coupled device, radiation effects, random telegraph signals

*oliver.lux@dlr.de; phone +49 8153 28 2426; www.dlr.de/pa/en/

**Now at: Max Planck Institute for Extraterrestrial Physics, Garching, Germany

1. INTRODUCTION

On 22 August 2018, the European Space Agency (ESA) launched the Aeolus mission, achieving a groundbreaking advancement in Earth observation. This mission provided near-real-time global wind profiles using ALADIN (Atmospheric Laser Doppler Instrument), the first Doppler wind lidar ever deployed in space [1]. The mission concluded its successful operations on 30 April 2023, surpassing its planned lifetime by 18 months, before the satellite reentered the Earth's atmosphere on 28 July 2023. Initially conceived as a technology demonstrator, Aeolus' wind observations have proven very valuable for numerical weather prediction models in major weather services around the world [2] as well as for a variety of scientific investigations, including the study of global-scale tropical waves [3] and the analysis of dynamic events in the stratosphere [4].

The high quality of the Aeolus data products was achieved despite the detrimental impact of dark current signal anomalies on single pixels, so-called "hot pixels", in the memory zone of the two Aeolus detectors, which were realized as accumulation charge-coupled devices (ACCDs). Over the nearly five-year mission period, a steadily increasing number of hot pixels was observed, eventually amounting to about 10% of all pixels in the two ACCD memory zones. Emergence of the first hot pixels during the in-orbit commissioning phase has induced variations of wind speed bias in certain altitudes of several meters per second. Consequently, a dedicated dark current calibration technique was introduced already a few months after launch and performed throughout the mission on a regular basis in order to mitigate the systematic errors and, hence, to ensure high data quality of the wind and secondary aerosol products of Aeolus [5].

Nevertheless, various signal anomalies on the individual hot pixels, such as random telegraph signal noise and sporadic shifts in the median dark current signal, occurring on different time scales, remain an issue for the reprocessing of the Aeolus data in phase F of the mission which covers all activities after the end of the operational phase including data analysis, reprocessing, reporting and archiving. Consequently, classification of the hot pixels with respect to the frequency and amplitude of dark current transitions is necessary for applying appropriate correction schemes. Moreover, identification of the root cause of the dark current anomalies is crucial with regard to current and future space missions that employ a similar detector technology based on CCDs. For this purpose, a series of dedicated tests was carried out in the last two months before the final switch-down of ALADIN in July 2023 to study, amongst others, the temperature dependence of the dark current rates for each detector pixel. The results obtained through these tests revealed the nature of the hot pixels and thus provided important insights for their mitigation in other spaceborne CCD detectors. This paper provides an overview of the performance of the Aeolus detectors in orbit, particularly emphasizing the different dark current anomalies observed throughout the mission.

2. INSTRUMENT DESIGN AND DETECTOR SPECIFICATIONS

The Aeolus satellite orbited Earth at about 320 km carrying ALADIN as its single payload. The Doppler wind lidar emitted 20 ns UV laser pulses at 354.8 nm wavelength and 50.5 Hz pulse repetition frequency. These pulses were backscattered by moving atmospheric particles, causing a Doppler shift. The same telescope that transmitted the UV laser beam also collected the backscattered light and directed it to a receiver with two channels: the Mie channel, which used a Fizeau interferometer for narrowband backscatter signals from clouds and aerosols, and the Rayleigh channel, which employed Fabry–Pérot interferometers for the broadband return from molecules. Both channels utilized ACCDs from Teledyne e2v (model CCD69) to accumulate signals from multiple laser pulses. The two ACCDs used in-flight were manufactured from the exact same wafer and offered 85% quantum efficiency at 355 nm, along with low readout noise, outperforming other detector types like avalanche photodiodes or photomultipliers available at the time of the instrument's development. Some specifications of the ACCDs and parameters describing their in-orbit performance are summarized in Table 1.

Each ACCD had an illuminated image zone with 16 × 16 pixels and a non-illuminated memory zone with 25 × 32 pixels with the latter being divided into 16 narrower transfer columns and 16 interleaved storage columns so that each pair of transfer/storage columns matches the pitch of image section's columns. The image zone and only the 16 storage columns of the memory zone are shown in Fig. 1. The signals transmitted through the Mie and Rayleigh spectrometers were recorded in the respective ACCD image zones where they were integrated over time based on predefined vertical range gate settings, with timings ranging from 2.1 to 16.8 µs, corresponding to 250 to 2000 m vertical sampling resolution. After each range gate integration period, charges in the image zone were moved downward row by row at 16 MHz, binned in the transfer row, and then pushed into the memory zone. This binning and transfer process, taking about 1.0 µs, was repeated for each range gate until the 25 rows of the memory zone were filled to produce the vertical profile.

Table 1. Specifications and important parameters of the ALADIN ACCDs measured on-ground and in-orbit.

Specification	**Value**
Type	Thinned backside-illuminated accumulation Si-CCD
Area	Image zone: 0.43 mm × 0.43 mm – 16 × 16 pixels Memory zone: 0.43 mm × 0.75 mm – 32 × 25 pixels
Pixel size	Image zone: 27 µm × 27 µm Memory zone: 30 µm × 13.5 µm
Temporal resolution	2.1 to 16.8 µs / 250 to 2000 m for atmospheric range gates (#1 to #24) 625 µs / 1250 µs / 3750 µs for solar background (range gate #25)
Parameter measured on-ground	**Value**
Quantum efficiency	0.85
Charge-transfer efficiency	0.999
Radiometric gain	Mie: 0.684 LSB/e^-; Rayleigh: 0.434 LSB/e^-
Parameter measured in-orbit	**Value**
Operating temperature	-30°C
Dark current signal rate (rms)	Mie: (0.72 ± 0.31) e^-s^{-1}; Rayleigh: (0.64 ± 0.31) e^-s^{-1}
Dark current signal noise (rms)	0.78 to 0.89 e^-
Readout noise (rms)	(5.6 ± 0.2) e^-

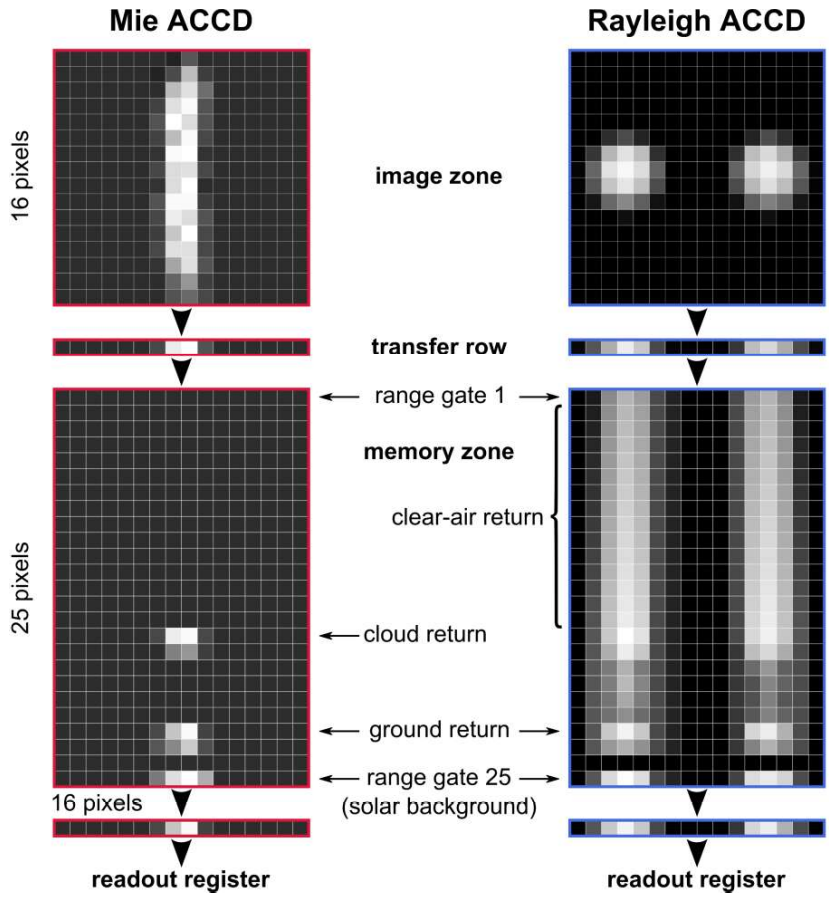

Figure 1. Schematic of the Aeolus ACCD design with exemplary signals measured in the image zone and transferred to the memory zone of the Mie (left) and Rayleigh (right) channel detectors.

The charges from the transfer columns were shifted to the corresponding pixels in the interleaved storage columns of the memory zone. After each sequence of laser shots constituting a measurement, the accumulated charges in the memory storage zone were read out at 48 kHz to minimize readout noise. The signal was converted into a voltage and sent to the detection electronics unit (DEU) for amplification and 16-bit digitization. An electronic offset voltage, called detection chain offset (DCO), was applied to prevent negative values during digitization. The DCO was generated by a special clocking sequence and quantified using two pre-scan and two post-scan pixels in each ACCD row. These pixels, containing minimal charges generated during readout, were used to correct the DCO in the 16 active pixels of each row. The amplified signals were then converted into units of least significant bits (LSB) with a radiometric gain of 0.684 LSB/e^- for the Mie channel and 0.434 LSB/e^- for the Rayleigh channel, respectively.

On-chip signal accumulation over a number of laser pulses (P) formed the so-called measurement scale. During ground processing, a set number of measurements (N) were combined into 12-second observations. For most of the Aeolus mission, P was set to 19 and N to 30. In December 2021, these settings were changed to 38/15 (P/N), and in April 2022 to 114/5 (P/N), in order to increase signal levels relative to the readout noise, thereby increasing the horizontal averaging length at the expense of horizontal resolution.

Unlike the first 24 atmospheric range gates, the integration time for row 25 of the memory zone was much longer to measure and correct for the solar background signal. Initially set at 3750 µs, this integration time was reduced to 1250 µs and then to 625 µs in April 2022 to prevent pixel saturation due to changes in P/N settings. In the following analysis, row and column indices denote pixel positions on the ACCDs, e.g., Mie [15,13] refers to row 15 and column 13 of the Mie ACCD memory zone with the counting starting at 1.

3. HOT PIXELS

In the early phase of the Aeolus mission, dark current signal anomalies in single hot pixels of the two ACCDs impacted the wind and aerosol data quality. Hot pixels are characterized by a permanent increase in dark current, mainly due to radiation-induced ionization or displacement damage. While ionization damages can be mitigated by effective shielding, displacement damage is caused by higher-energetic particles, mainly protons, that can pass through the shielding and the detectors, creating vacancy–interstitial pairs in the lattice. Apart from increased dark current, the stable displacement damages may introduce random telegraph signals (RTS) which manifest as abrupt step-like transitions between multiple discrete dark current levels occurring randomly and unpredictably.

Initially, the characterization of the dark current in the memory zone (DCMZ) was only planned at the mission's outset, prior to activating the laser. However, the increasing number of hot pixels necessitated regular dark current calibration throughout the mission. Therefore, the "down under dark experiment" (DUDE) was introduced as a special operation mode to measure dark current signals without lidar return contributions by adjusting the range gate timing settings such that the return signal would be acquired from beneath the Earth's surface while choosing locations with negligible solar background contributions [5]. As the mission progressed, DUDE measurements were performed more and more frequently (up to eight times per day starting from 30 October 2021) to address the growing number of hot pixels.

By the end of Aeolus's nearly five-year mission, there were a total of 75 hot pixels—41 on the Mie channel and 34 on the Rayleigh channel ACCD, respectively. This accounts for approximately 10% of all pixels in the two memory storage zones. The activation of hot pixels, where the dark current rate permanently exceeded the noise level, followed a nearly linear trend with successive hot pixel onsets occurring approximately every (23 ± 21) days. Figure 2 (a) illustrates deviations from this trend, notably in summer/autumn 2021 and between July and November 2022, when no new hot pixels emerged for 124 days. However, no correlation was found between hot pixel onset rate and space weather activity or any platform or instrument parameters. Interestingly, after the long gap in 2022, seven Rayleigh pixels became hot before another Mie hot pixel appeared. Since there is no correlation between these seven consecutive hits, either in terms of geolocation or location on the CCD, it appears to be coincidental and did not provide any further insight into the root cause.

The hot pixels were predominantly activated around the poles and the South Atlantic Anomaly (SAA) region, as illustrated in Fig. 2(b). The SAA, known for a weakened Earth's magnetic field at altitudes of 200 to 800 km, exposes the Aeolus satellite (at 320 km altitude) to increased radiation levels. Transient events, visible as signal spikes on the detectors, were found to be concentrated around the SAA, too, occurring about three times more frequently compared to other areas globally. However, these events affected only ~0.24% of all measurements, spread evenly across pixels on both detectors. Further investigation revealed that in about half of these events, multiple pixels exhibited simultaneous spurious intensity peaks, with some instances affecting more than 10 pixels concurrently, resulting in streaks on the memory zone that indicated the path of the grazing particles.

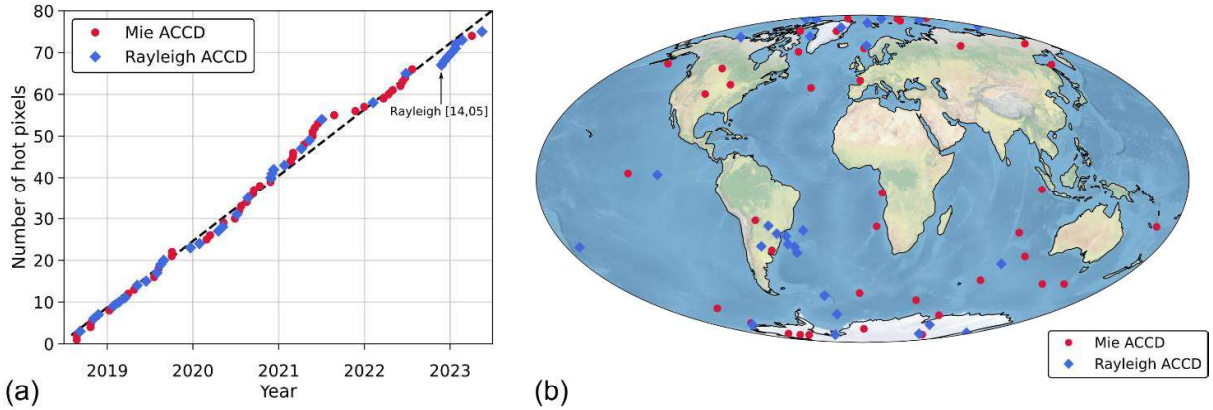

Figure 2. (a) Temporal progression of the number of hot pixels throughout the mission timeline. Mie hot pixels [16,15] and [24,03] were present before launch. (b) Geolocation of the satellite during the initial activation of individual hot pixels (only if data for the exact activation time is available). Mie and Rayleigh hot pixels are represented by red dots and blue diamonds, respectively. The map is displayed in Mollweide projection to ensure area equality.

Hot pixel classification and statistics

Data from approximately 8500 DUDE measurements taken throughout the entire mission period were used to analyze the dark current levels on each pixel of the memory zone of each ACCD, focusing on their temporal evolution. The solar background range gate 25 was neglected, as it had no significant impact on the wind results due to the long integration time and thus minimal contribution of dark current to the signal. Corrections for DCO and solar background were applied, and P/N settings changes during the mission were accounted for. A segmentation approach based on the Python ruptures package [6] was applied to the dark current time series to identify shifts in the dark current signal and to resolve discrete dark current levels of hot pixels that exhibit RTS behavior. The segmentation process was optimized by means of Monte Carlo simulations yielding robust statistics for the step size between RTS levels and their average lifetime, i.e., the average time span between successive RTS transitions.

The statistical analysis allowed for a classification of the 75 hot pixels according to their dark current characteristics, revealing that most of them (about three fourths) exhibit RTS behavior, with some displaying complex temporal signatures involving multiple RTS levels. Other hot pixels, in contrast, show rare shifts or slow drifts in the elevated dark current levels which are perceived as 1/f noise. Additionally, some pixels demonstrate a combination of RTS behavior and dark current shifts. The time series of three selected hot pixels belonging to the three aforementioned categories are shown in Fig. 3. Rayleigh pixel [08,10] was activated on 28 January 2020 when the dark current level suddenly increased from ~4 LSB to ~70 LSB. Following the onset, the mean dark current on this pixel remained stable with only small and rare steps until October 2022 when it dropped to ~33 LSB. Owing to their low activity, hot pixels of this category are not detrimental to the Aeolus data quality. Conversely, Mie pixel [19,15], which became hot on 1 May 2021, was characterized by frequent steps between seven RTS levels spanning a dark current range of about 200 LSB. The average time between two RTS transitions was 34 hours, corresponding to about 5 transitions per week. Such hot pixels may introduce large errors in the Aeolus data products, since a) the large dark current variations significantly affect the measured spectrometer responses and b) the comparatively short lifetime of the RTS levels increases the probability that the DCMZ correction based on the latest DUDE measurement is no longer appropriate. Some hot pixels show a combination of RTS fluctuations and shifts of the mean dark current. For instance, the dark current time series of Mie pixel [20,02] (bottom panel of Fig. 3) reveals a superposition of multi-level RTS with sporadic mean shifts.

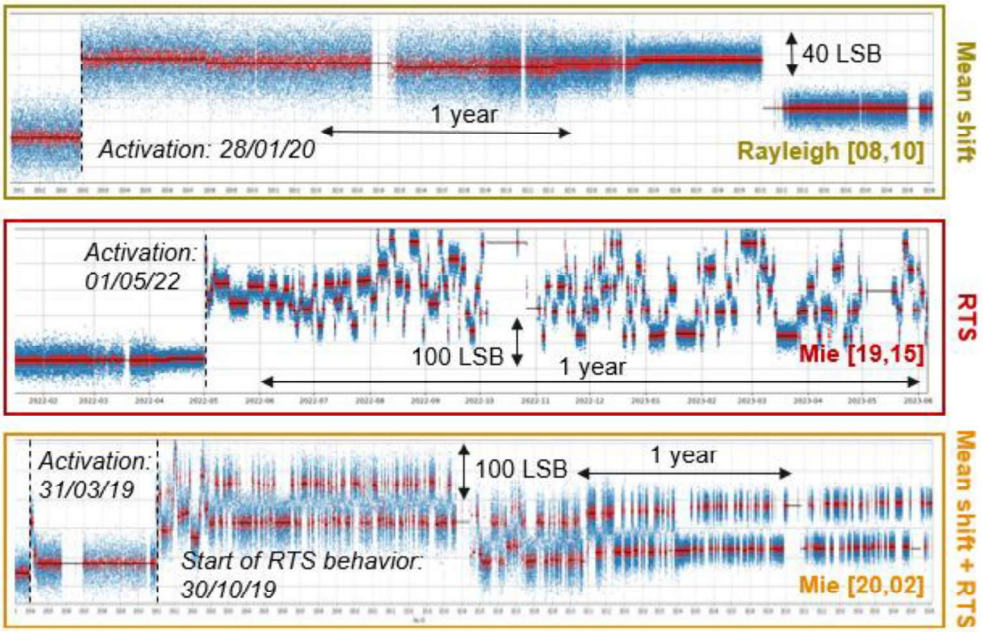

Figure 3. Time series of the dark current levels for three selected hot pixels with different temporal noise characteristics. Top: Rayleigh pixel [08,10] showing only very rare and comparatively small shifts of the mean dark current level; middle: Mie pixel [19,15] exhibiting multi-level RTS behavior with large steps of the dark current; bottom: Mie pixel [20,02] featuring a combination of two-level RTS transitions and a shift of the median dark current.

Overall, the analysis of all hot pixels yielded step sizes ranging from a few to hundreds of LSB (1 LSB ≈ 1.46 electrons / 2.30 electrons for the Mie and Rayleigh channel, respectively) and typical lifetimes of tens of hours to a few days. The correlation between these parameters and their distribution are depicted in Fig. 4, showing that shorter lifetimes, i.e., higher transition rates, tend to go along with larger step sizes (= transition amplitudes). It is interesting to note that the highest transition rates (>5 transitions per week) and largest transition amplitudes (>100 LSB) are almost exclusively found for Mie hot pixels with Rayleigh pixel [24,06] being the only exception.

The statistical parameters not only shed a light on the different characteristics of the hot pixels, but are also relevant for the reprocessing of the Aeolus data which is a major task during phase F of the mission from 2024 through 2028. The information about typical step sizes and lifetimes facilitates the distinction between real RTS transitions and atmospheric signal variations which may be of similar amplitude. This distinction is important when analyzing time series of raw signal levels measured on individual hot pixels with the goal to detect RTS steps and to introduce additional DCMZ correction files between wind measurements at times when there were no or only very few DUDE measurements, especially at the beginning of the mission [7].

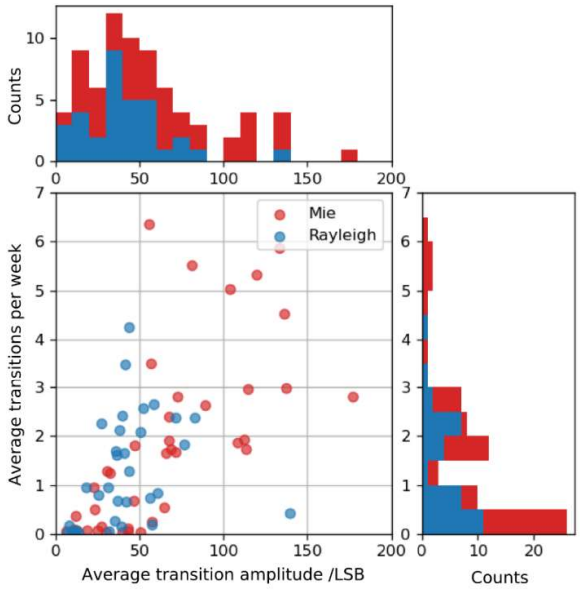

Figure 4. Results from the statistical analysis of all hot pixels with RTS characteristics during the mission period. The scatterplots show the correlation of the average RTS transition rate (y-axis) with the average transition amplitude (= RTS step size). The corresponding histograms of the two statistical parameters are displayed on the edges of the scatterplots with red bars representing Mie hot pixels and blue bars representing Rayleigh hot pixels.

The classification of the hot pixels can be observed in Fig. 5 which also depicts their positions within the memory zones of the Mie and Rayleigh ACCDs, along with their chronological order of activation. The maps reveal that the hot pixels did not occur randomly; instead, they exhibit notable clustering both spatially and temporally. For example, Mie hot pixels [17,05], [16,05], [17,07], and [18,04] are closely grouped and became active within a one-year period between June 2021 and June 2022. In contrast, no Mie hot pixels were detected in ACCD rows 21 through 23. Similarly, rows 2, 4, 12, 19, and 21 of the Rayleigh ACCD did not contain any hot pixels, while row 24 had as many as four. However, it should be kept in mind that two neighboring columns in the storage section are not exactly side by side in the silicon structure, but separated by an interleaved transfer column. Overall, 75% of the hot pixels displayed RTS behavior, with 29 out of 41 Mie hot pixels and 28 out of 34 Rayleigh hot pixels showed this characteristic. It should be noted that no annealing period of significant duration occurred during flight, which could have altered the RTS dynamics.

The two Rayleigh hot pixels [13,15] and [16,04] are highlighted in the figure because, besides demonstrating RTS features, they showed a charge storage anomaly that caused significant wind biases in the corresponding range gates despite the DCMZ correction based on the DUDE measurements. The cause of this anomaly is still under investigation and is outside the scope of this paper. However, it is addressed in another study on the ALADIN detector performance [8].

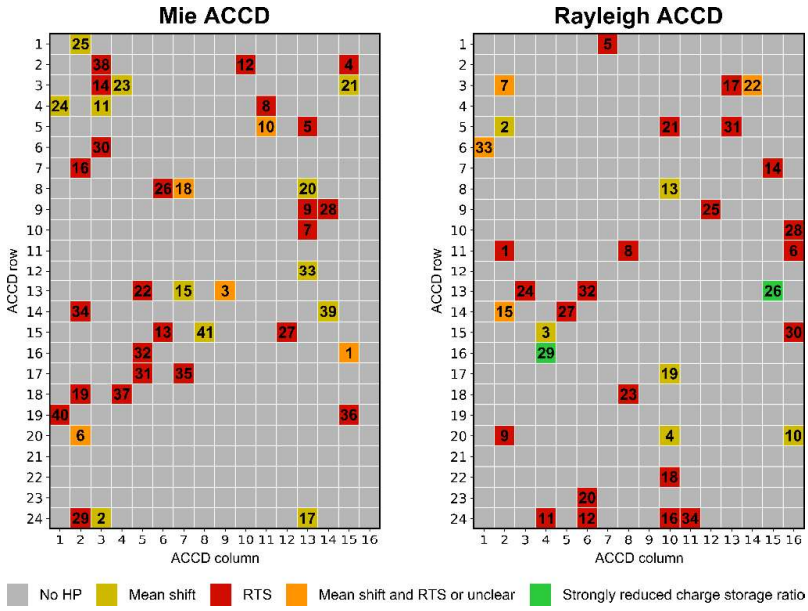

Figure 5. Map of hot pixels on the Mie ACCD (left) and the Rayleigh ACCD (right). The color coding refers to the classification of the individual hot pixel characteristics (see text), while the number indicates the chronological order of the activation on the respective detector.

4. END-OF-LIFE ACTIVITIES

Following the conclusion of the operational Aeolus mission in April 2023, a series of special in-orbit tests were conducted to address both instrument-related and scientific studies. These tests focused on Aeolus's performance, data reprocessing, and the preparation for other space lidar missions, including EarthCARE, which has been operating its atmospheric lidar ATLID since August 2024, and Aeolus 2, for which Phase B2 is set to begin in 2024. As part of these end-of-life (EOL) activities, the temperature dependence of dark current levels was examined, particularly on the pixels that had become hot during the mission. For this investigation, the ACCD temperature was increased from the nominal value of -30°C to -15°C in 5°C increments. The non-nominal temperatures of -25°C, -20°C, and -15°C were maintained for 4.5 hours each (approximately three orbits), allowing for a precise measurement of the dark current levels across all pixels of the memory zone. However, these periods were too brief to assess the temperature's effect on the RTS time constants of the hot pixels.

Temperature dependence of the dark current rates

Based on the test data from the ACCD temperature test, which was conducted on 15-16 May 2023, the median dark current rate for each individual pixel was calculated at the four temperature settings. The temperature dependence was then analyzed for both the nominal and hot pixels which was found to follow the Arrhenius law [9] on the small temperature range explored:

$$\mathrm{DC}(T) = \mathrm{DC}_0 \exp(-E_a/k_\mathrm{B}T), \tag{1}$$

where DC(T) is the measured dark current rate in electrons per second (e^-s^{-1}) depending on the absolute temperature T, DC_0 is a scaling constant, E_a is the activation energy for the dark current and k_B denotes the Boltzmann constant. Note that the radiometric gain factors of g_{Mie} = 0.684 LSB/e^- and g_{Ray} = 0.434 LSB/e^- were used for conversion from LSB to e^-. The above equation can be rewritten as follows:

$$\ln\big(\mathrm{DC}(T)\big) = -E_a/k_\mathrm{B}T + \ln(\mathrm{DC}_0). \tag{2}$$

Therefore, when plotting the natural logarithm of the measured dark current rates against the inverse temperature (Arrhenius plot), the points lay on a straight line and a linear fit can be applied to derive the activation energy.

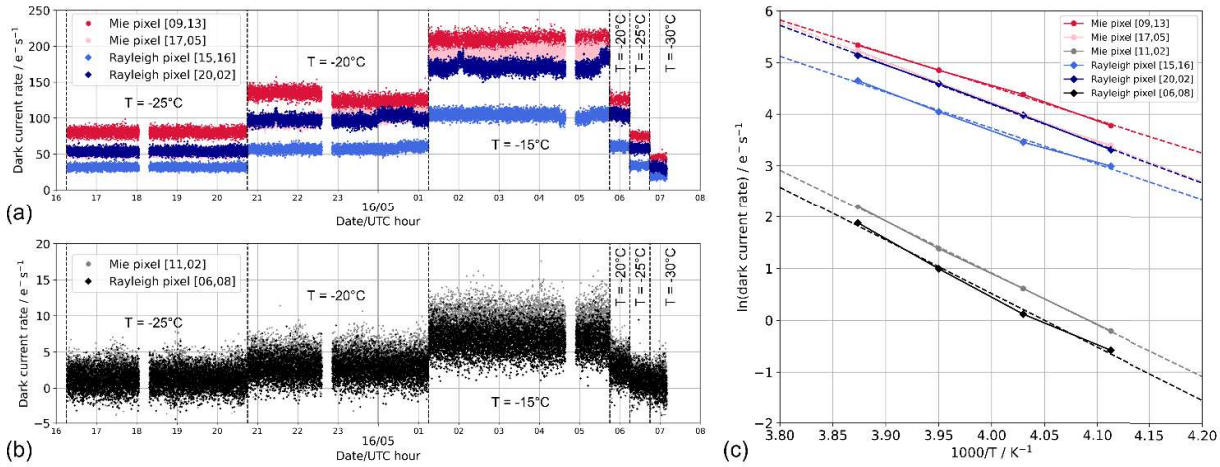

Figure 6. Temperature dependence of the ALADIN dark current rates. The time series of selected Mie and Rayleigh pixels during the ACCD temperature test on 15-16 May 2023 are shown in panels (a) and (b) for hot pixels and nominal pixels, respectively. The median values for each pixel and the four temperature settings are displayed in the Arrhenius plot in panel (c). The slope of the linear fit, indicated by the dashed lines, can be interpreted as the activation energy of the respective pixel.

The time series of the dark current rates measured during the test period for selected hot and normal pixels are depicted in Fig. 6(a) and (b), respectively. For the normal pixels, the subtraction of the noisy DCO and solar background from the raw data caused negative dark current rates for individual observations. Aside from the expected increase of the dark current rates with temperature, several signal steps were evident on the hot pixels, for instance on Rayleigh pixel [20,02] (dark blue diamonds in panel (a)). Based on the time series data, median values were calculated for all individual pixels over the periods covering the four different temperature settings to produce Arrhenius plots, as shown in Fig. 6(c). Linear fits were applied to determine the respective activation energies (in eV) for each pixel of the two ACCDs, resulting in the maps that are displayed in Fig. 7 together with the corresponding histograms for the two ACCDs.

The activation energies are relatively consistent across both ACCDs, with median values of $E_{a,Mie}$ = (0.87 ± 0.09) eV and $E_{a,Ray}$ = (0.87 ± 0.13) eV, respectively. The values are about 25% lower for the hot pixels, at $E_{a,Mie,hot}$ = (0.67 ± 0.13) eV and $E_{a,Ray,hot}$ = (0.65 ± 0.16) eV. This reduction is consistent with surface dark currents caused by radiation-induced displacement damages, supporting the assumption that the dark current anomalies are dominated by conventional hot pixels rather than clock-induced charges (CICs) which would be almost temperature-independent [10]. Specifically, the activation energies align closely with those of a phosphorus-vacancy (PV) dipole, which measures 0.70 eV, i.e., 0.44 eV below the silicon conduction band [11]. The occurrence of PV defects has also been observed in several studies on proton-irradiated CCD sensors [12].

Figure 8 depicts the dark current rates of all ACCD pixels at the nominal temperature of -30°C, as measured during the EOL test in May 2023. When excluding the hot pixels, the median rates account for $DC_{Mie,-30°C}$ = (0.72 ± 0.31) e^-s^{-1} and $DC_{Ray,-30°C}$ = (0.64 ± 0.31) e^-s^{-1}, respectively (see also Table 1). For the hot pixels, the dark current rates range from a few to several tens of electrons per second. The highest rate of ~90 e^-s^{-1}, determined for Rayleigh pixel [14,05], is outside the plot range of the histogram in Fig. 8.

The derived temperature dependence enabled extrapolation of the dark current rates to -50°C, the expected operational temperature for the detectors employed in the Aeolus-2 instrument. This yielded $DC_{Mie,-50°C}$ = (0.017 ± 0.012) e^-s^{-1} and $DC_{Ray,-50°C}$ = (0.015 ± 0.012) e^-s^{-1}, corresponding to a reduction by a factor of approximately 40 compared to -30°C for the normal pixels. Due to the smaller activation energies, and thus lower temperature sensitivities, of the hot pixels, their dark current rates are reduced by only a factor of about 17. Nonetheless, at -50°C, 47 of the 75 hot pixels (63%) would have dark current rates below 0.8 e^-s^{-1} comparable to the dark current rates of normal pixels at -30°C during the Aeolus mission. However, these hot pixels would still exhibit increased dark currents compared to normal pixels at -50°C. Aside from the reduced dark current rates, the RTS time constants are presumed to be longer at lower temperatures, although this could not be extrapolated from the EOL dataset due to the short test period.

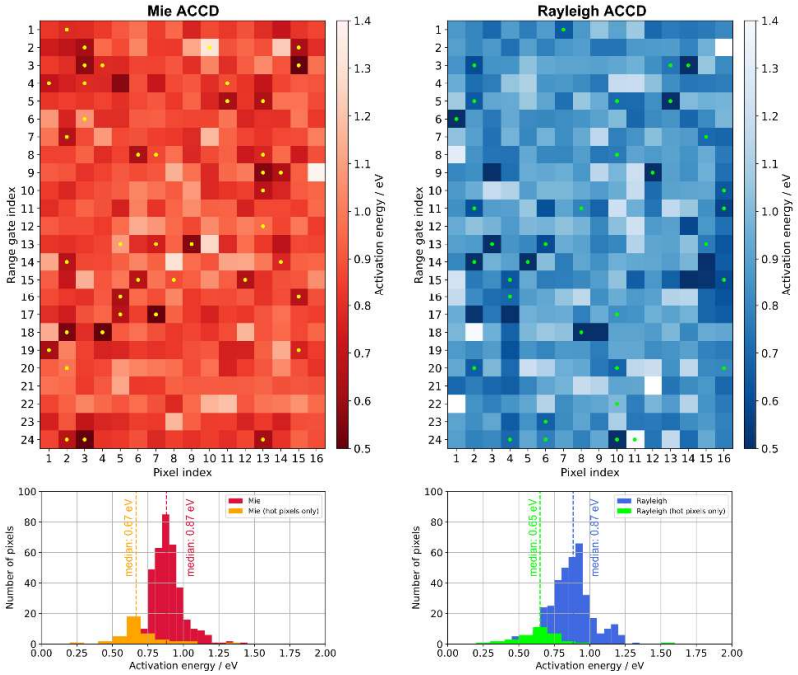

Figure 7. Activation energy of the pixels from the memory zone of the Mie (left) and Rayleigh ACCD (right). Hot pixels are indicated by dots. The corresponding histograms are shown in the bottom panels with median values of 0.87 eV (normal Mie pixels), 0.67 eV (Mie hot pixels), 0.87 eV (normal Rayleigh pixels) and 0.65 eV (Rayleigh hot pixels).

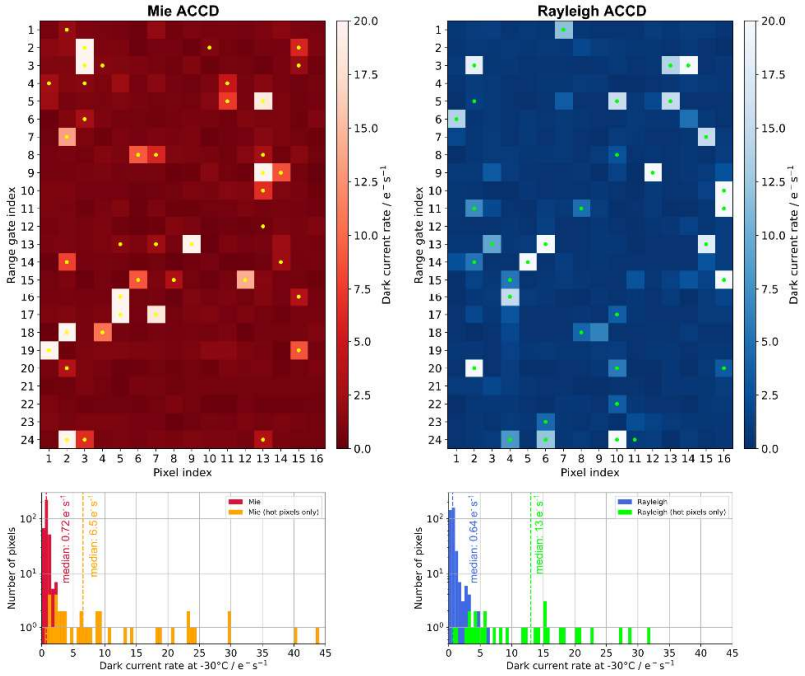

Figure 8. Dark current rates at -30◦C of the pixels from the memory zone of the Mie (left) and Rayleigh ACCD (right). Hot pixels are indicated by dots. The corresponding histograms are shown in the bottom panels with median values of 0.72 $e^{-}s^{-1}$ (normal Mie pixels), 6.5 $e^{-}s^{-1}$ (Mie hot pixels), 0.64 $e^{-}s^{-1}$ (normal Rayleigh pixels) and 13 $e^{-}s^{-1}$ (Rayleigh hot pixels).

The activation energies obtained from the Arrhenius plots were correlated with the dark current rates of the individual pixels, leading to the diagram shown in Fig. 9. The plot reveals that the activation energy decreases with the dark current rate. While the dependency is nearly linear in single logarithmic scale for most of the normal pixels (red and blue symbols), the data points for the hot pixels are more spread out (orange and lime symbols). Similar behavior was reported for proton-irradiated CCDs and traced back to field-enhanced emission in the bulk defects involving a significant lowering of the activation energy along with extreme increase in dark current rates [13,14]. Interestingly, the hot pixel with the highest dark current rate, Rayleigh pixel [14,05], was the one that emerged after the longest period without hot pixel activations between July and November 2022 (see also Fig. 2). The very low activation energy of 0.2 eV for Mie pixel [18,04] can be explained with RTS transitions during the EOL test affecting the median values for some of the temperature settings and hence the linear fit in the Arrhenius plot.

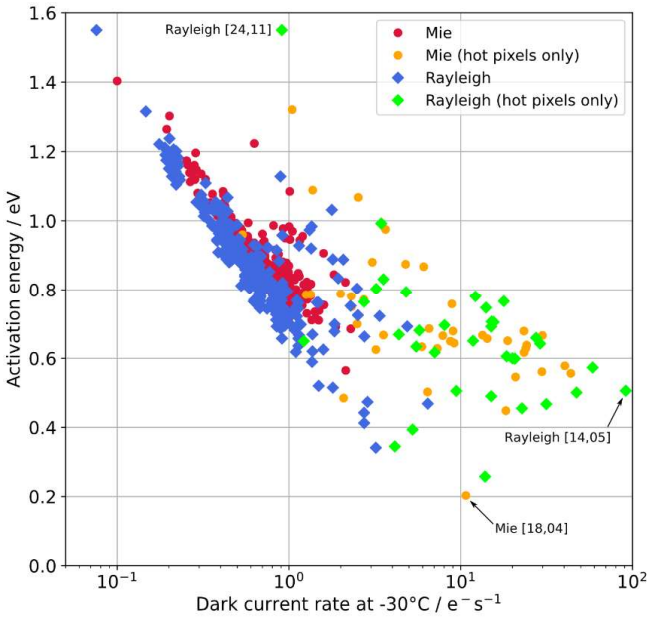

Figure 9. Activation energy versus dark current rate for all pixels of the Mie (circles) and Rayleigh ACCD (diamonds). Hot pixels are plotted in orange and lime color, respectively.

5. CONCLUSIONS AND OUTLOOK

The Aeolus mission demonstrated that a Doppler wind lidar can operate in space for several years, providing global wind profiles that significantly improve numerical weather forecasts. Despite detector anomalies, particularly 75 hot pixels on the ACCD memory zones, the mission succeeded by measuring dark current levels during laser operation in order to mitigate large systematic wind errors. The dark current calibrations additionally allowed for a classification of the hot pixels based on dark current characteristics, revealing that 76% exhibited RTS behavior with complex temporal signatures. Statistical analysis of the more than four-year-long dataset showed RTS step sizes from a few to hundreds of electrons and lifetimes of tens of hours to days. The statistics aid in distinguishing real RTS transitions from atmospheric signal variations which is crucial for the reprocessing of the Aeolus data products in phase F of the mission.

A dedicated in-orbit test, conducted after the operational phase of the Aeolus mission had ended, examined the temperature dependence of dark current levels, finding that hot pixels had temperature coefficients about 25% smaller than nominal pixels. This supported the theory that the enhanced dark current rates were due to radiation-induced displacement damages. Extrapolation to lower temperatures predicted dark current rates of less than 0.02 $e^{-}s^{-1}$ at -50°C, the expected operating temperature for Aeolus-2. This would reduce dark current rates for two-thirds of the hot pixels to levels comparable to normal pixels at -30°C, though RTS transitions and shifts in dark current rates may still pose challenges, albeit with less impact on wind results. The fact that the number of hot pixels and the impact of RTS fluctuations on the data quality exceeded expectations before the launch of Aeolus suggests that the on-ground irradiation testing methodology needs to be refined and extended for Aeolus-2.

The results of this work are highly relevant for other space lidar missions, such as EarthCARE and Aeolus-2, which use similar detector technology as Aeolus. For Aeolus-2, significant efforts are underway to address the impact of hot pixels, including the use of similar ACCDs from Teledyne e2v with the addition of a buffer store to reduce noise and enable continuous DCMZ measurements without sacrificing observation time. The number of atmospheric range gates will be increased from 24 to 66 to meet the demand for higher vertical resolution of wind profiles, despite a potential reduction in signal-to-noise ratio [15-17]. Other improvements for Aeolus-2 include UV-optimized anti-reflection coatings to enhance pixel quantum efficiency by 10% and operating at a lower temperature of -50°C to reduce thermal noise. Moreover, an airborne demonstrator is being considered to provide comprehensive testing of the new design features and advanced detectors of Aeolus-2.

The performance assessment of the Aeolus detectors is also relevant for other space instruments using CCD detectors. For example, hot pixels with RTS effects were observed on the GOMOS instrument on ENVISAT, affecting the ozone retrieval [18]. Similar temperature dependence analyses on other space instruments, such as the BRITE nanosatellite [19] and star trackers on the Solar Dynamics Observatory [20], have shown comparable results, indicating common radiation-induced defects.

REFERENCES

[1] Reitebuch, O., "The Spaceborne Wind Lidar Mission ADM-Aeolus," [Atmospheric Physics: Background – Methods – Trends], Springer, Berlin & Heidelberg, 815–827 (2012). https://doi.org/10.1007/978-3-642-30183-4_49

[2] Rennie, M. and Isaksen, L., "The NWP impact of Aeolus Level-2B winds at ECMWF," ESA Contract Report, (February 2024); https://doi.org/10.21957/d4ea1c09d4

[3] Ern, M., Diallo, M. A., Khordakova, D., Krisch, I, Preusse, P., Reitebuch, O., Ungermann, J., and Riese, M., "The quasi-biennial oscillation (QBO) and global-scale tropical waves in Aeolus wind observations, radiosonde data, and reanalyses," Atmos. Chem. Phys. 23(16), 9549–9583 (2023). https://doi.org/10.5194/acp-23-9549-2023

[4] Banyard, T. P., Wright, C. J., Osprey, S. M., Hindley, N. P., Halloran, G., Coy, L., Newman, P. A., Butchart, N., Bramberger, M., and Alexander, M. J., "Aeolus wind lidar observations of the 2019/2020 quasi-biennial oscillation disruption with comparison to radiosondes and reanalysis," Atmos. Chem. Phys. 24(4), 2465–2490 (2024). https://doi.org/10.5194/acp-24-2465-2024

[5] Weiler, F., Kanitz, T., Wernham, D., Rennie, M., Huber, D., Schillinger, M., Saint-Pe, O., Bell, R., Parrinello, T., and Reitebuch, O., "Characterization of dark current signal measurements of the ACCDs used on board the Aeolus satellite," Atmos. Meas. Tech. 14(7), 5153–5177 (2021). https://doi.org/10.5194/amt-14-5153-2021

[6] Truong, C., Oudre, L., and Vayatis, N., "Selective review of offline change point detection methods," Signal Processing, 167, 107299 (2020); https://doi.org/10.1016/j.sigpro.2019.107299

[7] Weiler, F., "Detecting hot pixel induced steps in the Aeolus atmospheric signals," Master thesis, University of Innsbruck, Innsbruck (2021).

[8] Lux, O., Reichert, R., Lemmerz, C., Masoumzadeh, N., Wernham, D., Krisna, T. C., Marchais, D., Bell, R., Parrinello, T., and Reitebuch, O., "CCD detector performance of the space-borne Doppler wind lidar ALADIN during the Aeolus mission," Appl. Opt. 63(25), 6754–6775 (2024). https://doi.org/10.1364/AO.532217

[9] Widenhorn, R., Blouke, M. M., Weber, A., Rest, A., and Bodegom, E., "Temperature dependence of dark current in a CCD," Proc. SPIE 4669, Sensors and Camera Systems for Scientific, Industrial, and Digital Photography Applications III; 193–201 (2002); https://doi.org/10.1117/12.463446

[10] Bush, N., Heymes, J., Hall, D., Holland, A., and Jordan, D. "Measurement and optimization of clock-induced charge in electron multiplying charge-coupled devices," J. Astron. Telesc. Instruments, Syst., 7(1), 016002 (2021). https://doi.org/10.1117/1.JATIS.7.1.016002

[11] Janesick, J. R. "Scientific Charge-coupled Devices," SPIE Press (2001). https://doi.org/10.1117/3.374903

[12] Hopkinson, G., "Radiation effects on solid state imaging devices," Radiat. Phys. Chem., 43(1/2), 79—91 (1994). https://doi.org/10.1016/0969-806X(94)90203-8

[13] Hopkinson, G. R., "Radiation-induced dark current increases in CCDs," [RADECS 93. Second European Conference on Radiation and its Effects on Components and Systems (Cat. No.93TH0616-3)], 401–408 (1994). https://doi.org/10.1109/RADECS.1993.316569

[14] Hopkinson, G. R. and Mohammadzadeh, A., "Comparison of CCD damage due to 10- and 60-MeV protons," IEEE Trans. Nucl. Sci., 50(6), 1960–1967 (2003). https://doi.org/10.1109/TNS.2003.821409

[15] Heliere, A., Wernham, D., Mason, G., Villele, G. de, Corselle, B., Lecrenier, O., Belhadj, T., Bravetti, P., Arnaud, S., Bon, D., Lingot, P., Foulon, R., Marchais, D., Olivier, M., D'Ottavi, A., Verzegnassi, F., Mondello, A., Coppola, F., Landi, G., Hoffmann, H.-D., Esser, D., Perez Prieto, L., Wührer, C., Rivers, C., and Bell, R., "Status of Aeolus-2 mission pre-development activities", Proc. SPIE 12777, International Conference on Space Optics; 1277709 (2023); https://doi.org/10.1117/12.2688794

[16] Wernham, D., Heliere, A., Mason, G., et al., "Status of Aeolus-2 pre-development activities," Aeolus 3rd Anniversary Conference, Taormina, Italy, 28 March–1 April 2022.

[17] Pratlong, J., "LiDAR Technologies and Detector Solutions," [Space-based Lidar Remote Sensing Techniques and Emerging Technologies]. Springer Aerospace Technology, Springer, Cham (28 April 2024); https://doi.org/10.1007/978-3-031-53618-2_34

[18] Keckhut, P., Hauchecorne, A., Blanot, L., Hocke, K., Godin-Beekmann, S., Bertaux, J.-L., Barrot, G., Kyrölä, E., van Gijsel, J. A. E., and Pazmino, A., "Mid-latitude ozone monitoring with the GOMOS-ENVISAT experiment version 5: the noise issue," Atmos. Chem. Phys., 10(23), 11839–11849 (2010). https://doi.org/10.5194/acp-10-11839-2010

[19] Popowicz, A.,"Analysis of Dark Current in BRITE Nanostellite CCD Sensors," Sensors 18(2), 479 (2018). https://doi.org/10.3390/s18020479

[20] Felikson, D., Ekinci, M., Hashmall, J., and Vess, M.,"On-Orbit Solar Dynamics Observatory (SDO) Star Tracker Warm Pixel Analysis," AIAA Guidance, Navigation, and Control Conference, Portland, Oregon, USA, 08/08 - 11/08/2011. https://ntrs.nasa.gov/citations/20110007815